Research Square

Preprints are preliminary reports that have not undergone peer review.
They should not be considered conclusive, used to inform clinical practice,
or referenced by the media as validated information.

Intrusive UWB/IMU Joint Measurement Method for Internal Trajectory Reconstruction in Dense Granular Flows

Yan-wen Chen
University of Shanghai for Science and Technology
Zhi-Peng Chi
University of Shanghai for Science and Technology
Hui Yang
Shanghai University of Medicine and Health Sciences
Ran Li
ran89@usst.edu.cn

University of Shanghai for Science and Technology

Research Article

Keywords: UWB/IMU fusion, intrusive measurement sphere, factor graph optimization, trajectory reconstruction, dispersion degradation

Posted Date: November 13th, 2026

DOI: https://doi.org/10.21203/rs.3.rs-11146502/v1

License: This work is licensed under a Creative Commons Attribution 4.0 International License.
Read Full License

Additional Declarations: No competing interests reported.

Intrusive UWB/IMU Joint Measurement Method for Internal Trajectory Reconstruction in Dense Granular Flows

Yan-wen Chen[1], Zhi-Peng Chi[1], Hui Yang[2,1],Ran Li[1*]

1. *School of Optical-Electrical and Computer Engineering, University of Shanghai for Science and Technology, Shanghai, 200093, China*

2. *College of Medical Instrumentation, Shanghai University of Medicine & Health Sciences, Shanghai 201318, China*

Corresponding author: Ran Li. E-mail: ran89@usst.edu.cn

Abstract

To address the challenge of continuously acquiring internal motion information in dense granular flows under particle occlusion and optically inaccessible conditions, this paper proposes an internal trajectory reconstruction method for dense granular flows based on factor graph optimization, using an intrusive Ultra-Wideband (UWB)/Inertial Measurement Unit (IMU) system, and tests and validates the algorithm in inclined chutes under different burial states, particle size gradations, and water-containing conditions. Results show that this method can characterize the main migration process of the measurement sphere along the chute direction with temporal consistency in different granular environments, which significantly suppresses trajectory dispersion. Data show that trajectory dispersion does not exhibit a monotonic correlation with granular environment complexity—IMU dynamic response decreases while trajectory dispersion increases, and this reverse trend reveals that the fundamental cause of self-consistency degradation is not weakened inertial measurement dynamic response, but rather motion path uncertainty caused by contact network structure. The proposed method provides a new measurement approach and analysis method for quantitatively analyzing the dispersion degradation law and path uncertainty of granular flow motion from an internal perspective.

Keywords: UWB/IMU fusion; intrusive measurement sphere; factor graph optimization; trajectory reconstruction; dispersion degradation

1. Introduction

Acquiring internal motion information of granular flows is both a fundamental rheological problem and a key technical challenge in optimizing industrial conveying devices and predicting the motion of geological hazards. However, experimental measurement of granular flow internal motion has long faced the "optically inaccessible" challenge. Traditional optical methods (PIV/PTV, etc.) cannot penetrate the surface layer to obtain internal motion information [1, 2, 3], while X-ray high-speed radiography [4], positron emission particle tracking [5], and magnetic resonance imaging [6] can provide internal three-dimensional motion information, but their high experimental cost and stringent environmental requirements make them difficult to apply in complex working conditions. In recent years, the "intrusive particle" technique—embedding sensors into solid carriers with a certain size and density to indirectly characterize the internal motion features of granular systems through carrier motion—has become a viable approach for internal measurement of granular flows due to its deployment flexibility and repeatability.

Inertial measurement units have been widely used in granular motion measurement. Köstler et al. [7] quantitatively analyzed the energy dissipation law of projectiles in granular media through embedded inertial sensing; Jiao et al. [8] designed spherical particles with built-in IMUs and completed kinematic equivalence calibration through free-fall and inclined-plane rolling; Xie et al. [9] developed smart sediment particles that achieved single-particle-level transport process monitoring in fluvial flumes. Černilová et al. [10] validated the application potential of IMU sensors for in-situ three-dimensional motion monitoring of particulate matter. However, IMUs estimate position and attitude by integrating acceleration and angular velocity, with errors accumulating over time. Significant drift can occur within tens of seconds in granular flow experiments. Some studies have attempted to introduce external magnetic field localization or acoustic assistance [26, 27], but the operating range is typically limited to meter-scale, making it difficult to cover commonly used spatial scales. Therefore, while maintaining the high sampling rate and dynamic response capture capability of IMUs, introducing an external positioning method that provides absolute

spatial reference to suppress inertial integration drift is key to advancing intrusive particle methods toward precise quantification.

Ultra-Wideband (UWB) wireless ranging technology measures the distance between transmitter and receiver using the time-of-flight (ToF) of nanosecond-level pulse signals, offering centimeter-level ranging accuracy, high refresh rate, and a certain penetration capability [11]. This technology provides new possibilities for overcoming the long-term drift problem of purely inertial solutions. Sui et al. [12] introduced non-line-of-sight (NLOS) angle discrimination and map constraints to enhance positioning robustness; Leitch et al. [13] reviewed the progress of WiFi/BLE/UWB/IMU indoor positioning technologies and clarified that UWB modules can fundamentally suppress the error divergence of inertial integration, with the high-frequency sampling characteristics of IMUs ensuring the continuity of motion trajectories when UWB signals are lost.

In terms of fusion algorithms, there are primarily two technical routes: recursive filtering and deep learning assistance. The recursive filtering route is represented by the Extended Kalman Filter (EKF) and Unscented Kalman Filter (UKF) [11, 14]. Cheng et al. [15] proposed a variational Bayesian-based INS/UWB fusion error compensation method; Wang et al. [16] improved indoor positioning accuracy through NLOS classifier-assisted compensation. However, the common limitation of these recursive methods is that state estimation relies only on current and historical observations. When particle occlusion causes continuous degradation of UWB ranging quality over multiple frames, the filter covariance grows rapidly, and the trajectory is prone to unrecoverable divergence. In the deep learning assistance route, Ren et al. [17] used attention-based LSTM networks to learn the nonlinear mapping between UWB ranging and positioning results; Wang et al. [18] proposed an xLSTM-based multimodal residual fusion method; Zhou et al. [19] and Liu et al. [20] employed deep learning optimization and neurodynamic robust adaptive algorithms, respectively, to mitigate NLOS effects. Additionally, Guo et al. [28] used hardware-accelerated fuzzy clustering to optimize UWB positioning; Lee et al. [29] constructed an outdoor UWB dataset in LOS/NLOS environments; Tu et al. [32] proposed an NLOS identification method based on neural

network multi-source fusion. Cheng et al. [31] applied an INS/UWB multi-sensor fusion scheme to indoor LOS/NLOS mixed environments, verifying the complementary advantages of multi-sensor fusion in complex propagation conditions. These data-driven methods perform well in scenarios covered by training data, but their generalization capability to unseen conditions such as particle size variations and moisture content changes in granular flows remains uncertain.

Factor graph optimization, as a batch state estimation framework, has received widespread attention in multi-sensor fusion positioning in recent years [21, 22]. Its core idea is to transform state estimation into a global nonlinear least-squares problem, simultaneously solving for the states at all time instants through iterative optimization. Compared with recursive filtering, factor graphs have three key advantages: backward smoothing—future observations can retrospectively correct past state estimates; flexible constraint modeling—different types of sensors and physical priors can be expressed in a unified framework; and inherent robustness—abnormal observations are soft-suppressed rather than hard-rejected through robust kernel functions. Existing studies have shown that in indoor NLOS scenarios, factor graph approaches outperform recursive filtering approaches in both error and robustness [23, 24]. However, the complex granular flow field poses three main challenges to this algorithm. First, occlusion in granular media is dynamically changing—particle flow, collision, and rearrangement cause the propagation path to continuously evolve, leading to abnormal jumps and systematic biases in UWB ranging, which is fundamentally different from the stable NLOS caused by building walls. Second, the motion of the measurement sphere is not free-space rigid-body motion, and recursive filtering methods lack sufficient stability for such continuous weak-observation scenarios [14, 30]. Third, there is coupling between the damping effect of granular media on high-frequency motion and UWB signal attenuation—in high-moisture or fine-particle media, weakened IMU response is often accompanied by synchronous degradation of UWB ranging quality, introducing new trade-offs for fusion strategies.

Addressing the above challenges, this paper selects factor graph optimization as the core framework for UWB/IMU fusion, using an inclined chute granular flow as the

experimental platform to investigate the three-dimensional trajectory reconstruction and dispersion degradation law of embedded measurement spheres in complex granular environments. Based on the design of the UWB/IMU measurement system, this paper introduces adaptive NLOS weights, Gaussian process (GP) smoothing priors, height anchoring, and zero-velocity constraints to enhance trajectory stability under occlusion, weak observation, and stopping phases. Compared with the EKF tightly coupled method under various burial states, particle size gradations, and moisture conditions, the proposed method demonstrates significantly superior performance in both trajectory reconstruction accuracy and robustness.

2. Materials and Methods

2.1 Experimental System and Measurement Device

2.1.1 Experimental System

The experimental system consists of a transparent inclined chute, granular materials, an intrusive UWB/IMU measurement sphere, an external UWB base station network, video acquisition equipment, and a data processing terminal (Fig. 1). The chute has a length of approximately 700 mm, a right-end height of approximately 520 mm, and an inclination angle of 20°. The right side of the chute is the granular filling zone, separated by a baffle, while the left side is the empty chute zone. The coordinate system is defined with the X-axis along the chute sliding direction, the Y-axis as the chute width direction, and the Z-axis vertically upward. Due to the limited chute width, Y-direction displacement is relatively small, and the analysis focuses on the X-Z plane.

Four UWB base stations (A0, A1, A2, A3) are arranged around the platform. The measurement sphere is equipped with a built-in UWB tag and IMU. After receiving UWB ranging signals, the base stations transmit them to the data processing terminal via a data link. A video acquisition device is positioned above the platform to synchronously record the motion process of the measurement sphere. The system combines UWB ranging with video acquisition to monitor the trajectory and position changes of the measurement sphere in the inclined granular system.

Dry particle experiments use polyoxymethylene (POM) particles with a density of 1.41 g/cm³. Three schemes are designed: d_s = 10 mm, d_l = 15 mm, and a mixed

gradation with a mass ratio m_s/m_l = 1.5. The total mass of particles in each group is kept constant at 2044 g. The wet condition is achieved by adding 300 mL of purified water (density 1 g/cm³) to the dry particles, thoroughly stirring to ensure uniform moisture distribution, and then allowing the mixture to settle. The gravimetric moisture content is 12.8% (pendular state).

Before the experiment begins, the granular material is placed at the high end of the chute and restrained by a baffle, and the measurement sphere is placed at a fixed initial position according to the predetermined condition. After the baffle is instantaneously withdrawn, the particles slide down the chute under gravity and drive the measurement sphere into motion. A single experiment lasts approximately 3 s, covering the complete process of initial rest, startup, flow migration, deceleration and settling, and final stop.

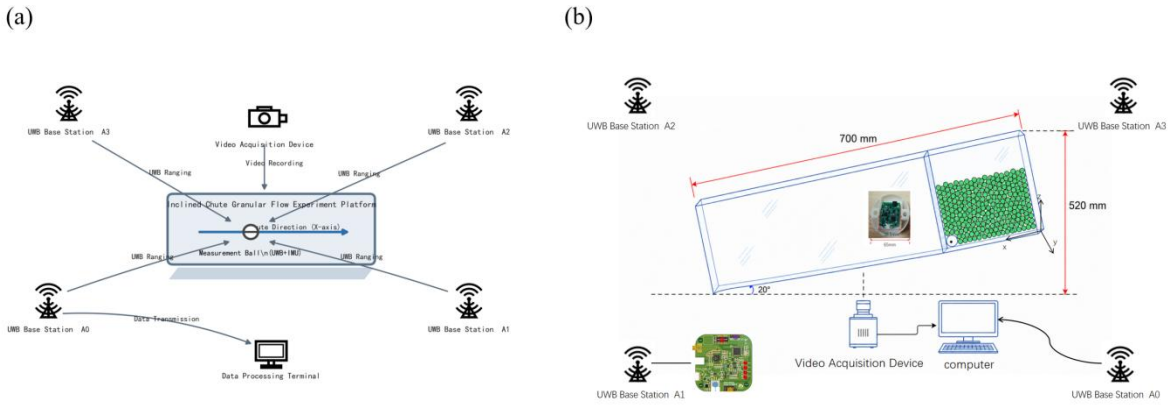


Fig. 1. Schematic of the inclined chute granular flow experimental platform—system composition and structural dimensions. (a) System composition and data link; (b) Chute structural dimensions and particle filling.

The experiments are divided into three groups based on granular system characteristics and variable hierarchy: Condition Groups 1, 2, and 3 respectively investigate the effects of particle coverage degree, particle gradation, and medium on the measurement results. A total of 6 independent experimental conditions are covered, with 30 repeated experiments conducted for each condition, totaling 180 experiments, as shown in Table 1.

Table 1. Experimental Condition Settings

Group	Condition	Particle Size	Burial State	Moisture	Repetitions
1	Unburied	10 mm	Unburied	Dry	30
1	Half-buried	10 mm	Half-buried	Dry	30
1	Fully buried	10 mm	Fully buried	Dry	30
2	10 mm, fully buried	10 mm	Fully buried	Dry	30
2	15 mm, fully buried	15 mm	Fully buried	Dry	30
2	Mixed gradation	10+15 mm	Fully buried	Dry	30
3	10 mm, wet	10 mm	Fully buried	Wet	30

During data processing, time synchronization, unified resampling, and trajectory reconstruction are performed for each group of experiments. On this basis, the experimental results that best reflect the typical characteristics of each condition are selected for presentation. Subsequent figures and tables in the paper are presented using typical experimental data, and the data selection method is not reiterated.

2.1.2 Measurement Sphere and UWB/IMU Measurement System

The measurement sphere uses a white resin shell with a diameter of approximately 65 mm and a total mass of 76.4 g. It integrates a UWB module, an IMU, an STM32F103CBT6 main control unit, and a 3.7 V lithium battery (Table 2). Four UWB base stations are deployed externally: A0 (0, 0, 1.9) m, A1 (4, 0, 2.2) m, A2 (4, 5, 2.2) m, and A3 (0, 5, 2.2) m.

Table 2. Intrusive Measurement Sphere and Main Sensor Parameters

Parameter	Specification/Value	Parameter	Specification/Value
Sphere diameter	65 mm	UWB module	DW3210

Total mass	76.4 g	UWB frequency	60 Hz
Main control unit	STM32F103CBT6	IMU model	Movella/Xsens MTi-1
Battery	3.7 V Li-ion	IMU frequency	120 Hz
Number of base stations	4	Ranging accuracy	±10 cm

The UWB module in Table 2 uses the DW3210 chip and transmits UWB pulses to external base stations at a frequency of 60 Hz. Its measurement principle is based on the time-of-flight (ToF) of nanosecond-level pulse signals: after receiving the signal, the base station calculates the round-trip time and multiplies it by the speed of light to obtain the straight-line distance between the transmitter and receiver. The nominal accuracy of a single ranging measurement is approximately ±10 cm, with actual accuracy affected by factors such as signal bandwidth, multipath propagation, and medium attenuation. The known coordinates of the four base stations constitute a three-dimensional spatial reference, and the four distance observations at each instant provide geometric constraints for the position solution of the measurement sphere.

The IMU module in Table 2 uses the Movella/Xsens MTi-1 series, simultaneously acquiring three-axis acceleration and angular velocity at 120 Hz. The accelerometer measures the specific force including the gravity vector; the gyroscope measures the body angular velocity. Initial attitude estimation is performed using the Mahony complementary filter [25]: the gravity direction observed by the accelerometer serves as the reference for attitude error, and the low-frequency drift of gyroscope angular velocity integration is corrected through proportional-integral feedback:

$$\dot{\hat{R}} = \hat{R}\left[\omega_m - \hat{b}_\omega + K_P \cdot e\right]_\times \tag{1}$$

where $\hat{R} \in SO(3)$ is the estimated attitude rotation matrix, ω_m is the gyroscope measurement, $\hat{b}_\omega$ is the estimated gyroscope bias, $e = \left(\hat{R}^{\mathrm{T}} e_3\right) \times (a_m / \|a_m\|)$ is the

gravity direction error ($e_3 = [0,0,1]^{\mathrm{T}}$, a_m is the normalized accelerometer measurement), $[\cdot]_\times$ is the skew-symmetric matrix operator, and $K_P = 0.6$ is the proportional gain. To avoid centrifugal acceleration interference with attitude estimation during vigorous motion, acceleration correction is enabled only when the accelerometer norm falls within the range of 7.5–12.5 m/s². After attitude estimation, the body acceleration is transformed to the world frame and the gravity component is removed: $a^{(world)} = \hat{R} \cdot a^{(body)} - [0,0,g]^{\mathrm{T}}(g = 9.81m/s^2)$. After this processing, the world-frame acceleration reflects the actual motion acceleration of the measurement sphere, and the angular velocity reflects its rotational state.

The sampling frequencies of the UWB, IMU, and video systems are 60 Hz, 120 Hz, and 60 Hz, respectively. Time alignment is performed at key event points such as particle release, the onset of significant motion of the measurement sphere, and the stopping state, followed by resampling to a unified time axis (step size 10 ms). IMU raw data are corrected for zero bias during the stationary segment before being used for dynamic response analysis. The video reference trajectory is mainly obtained from the sidewall view: pixel coordinates are first converted to physical coordinates using a calibration board, and then transformed to the experimental coordinate system through coordinate system transformation. The complete processing pipeline from raw multi-source data acquisition to final trajectory reconstruction is shown in Fig. 2.

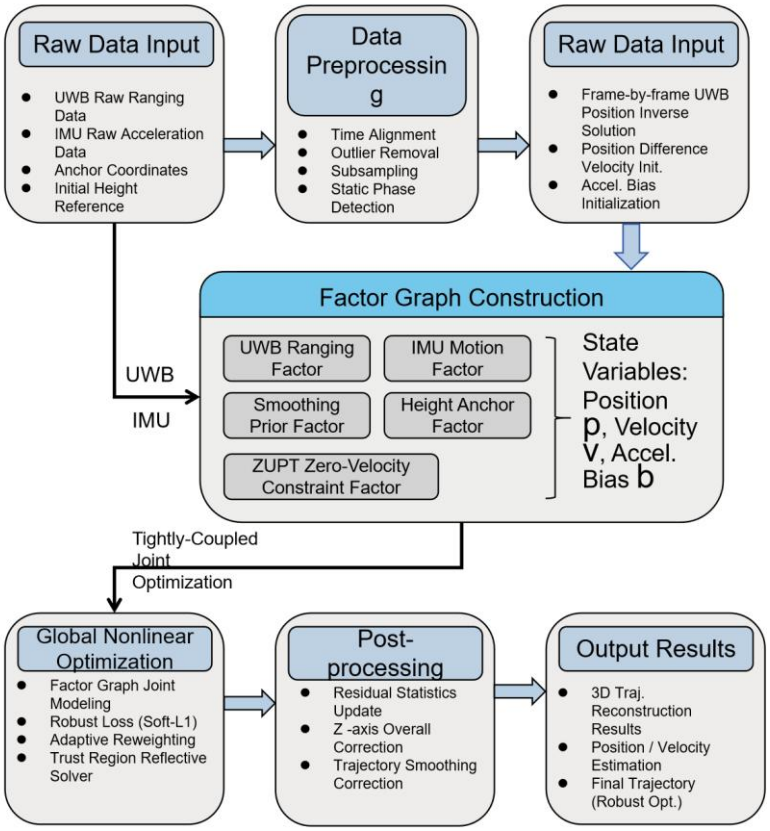


Fig. 2. Multi-source data acquisition and trajectory reconstruction workflow.

2.2 Factor Graph Trajectory Reconstruction Algorithm

2.2.1 Factor Graph Model and Constraint Construction

k At each time step k, the state is a 9-dimensional vector composed of positionp_k, velocity v_k, and acceleration bias $b_{a,k}$:

$$x_k = \begin{bmatrix} p_k \\ v_k \\ b_{a,k} \end{bmatrix} \in R^9 \tag{2}$$

The state vector to be estimated for the entire trajectory is $X = [x_0^\top, \dots, x_{N-1}^\top]^\top \in R^{9N}$. The optimization objective is a weighted nonlinear least-squares problem:

$$\min_X \sum_{i \in C} \rho\left(\| r_i(X) \|_{\Omega_i}^2 \right) \tag{3}$$

r_i where r_i is the residual of the i-th factor, Ω_i is the information matrix$\rho(\cdot) is\ the\ Soft-L1$, and $\rho(\cdot)$ is the $9N$ robust kernel. The factor graph consists of$p_k, v_k, b_{a,k}$state nodes:

1) Motion factors: connect adjacent frames x_i and x_j, transmitting IMU pre-integration or constant-velocity kinematic constraints;

2) UWB ranging factors: connect p_k to base station A_a, providing absolute distance observations with adaptive NLOS weights for dynamic adjustment;

3) GP smoothing factors: constrain acceleration consistency and jerk consistency across three consecutive frames, suppressing non-physical high-frequency jitter in particle-damped environments;

4) Auxiliary factors: including Z-axis height anchoring (strong constraint for the first frame, soft constraint for subsequent frames) and ZUPT zero-velocity constraint (forcing velocity to zero when stationary state is detected);

5) Boundary prior factors: imposing initialization priors on the position and velocity of the first and last frames to prevent endpoint drift.

The factor graph structure is illustrated in Fig. 3. state nodes $x_k = [p_k; v_k; b_{a,k}]$ are arranged along the time axis, and the five types of factor edges connect the corresponding nodes—motion factors connect adjacent frames (solid edges), UWB ranging factors connect position nodes to each base station A_a(dashed edges), GP smoothing factors connect across three consecutive frames (curved edges), Z-axis anchoring and ZUPT auxiliary factors act on the corresponding state nodes (self-loop edges), and boundary prior factors act on the first and last frames (self-loop edges).

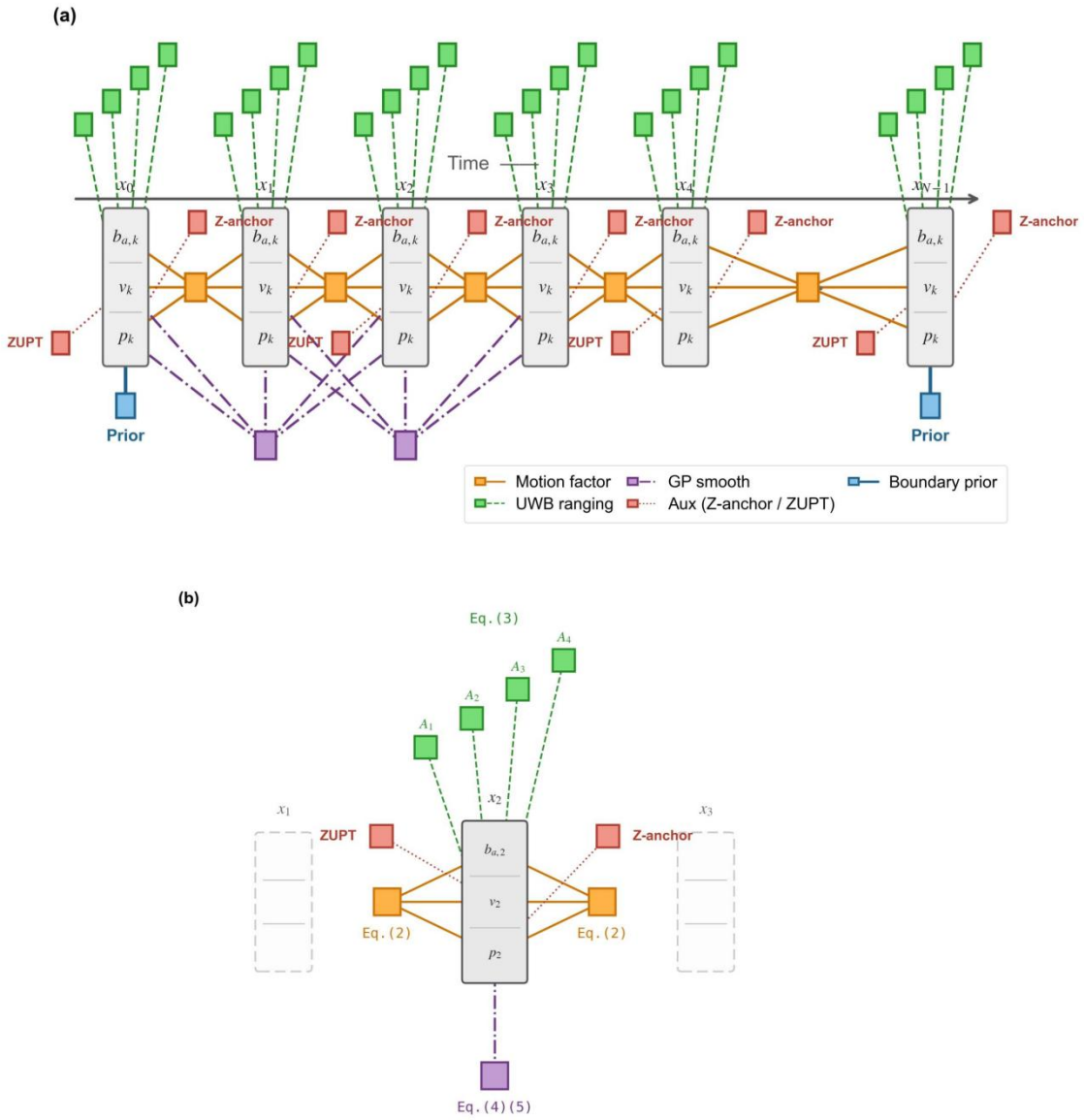


Fig. 3. Factor graph structure schematic. (a) Overall factor graph structure; (b) Local magnification.

Each constraint module addresses different error sources in granular flow internal measurement, and their independent contributions and synergistic effects are verified through ablation experiments.

For adjacent i and $j = i + 1(\Delta t)$, when the world-frame acceleration a is available, the motion_imu model is used:

$$r_{i\to j}^{\text{imu}} = \begin{bmatrix} p_j - \left(p_i + v_i \Delta t + \frac{1}{2(a^{-} - b_{a,i})\Delta t^2}\right) \\ v_j - \left(v_i + (a^{-} - b_{a,i})\Delta t\right) \\ b_{a,j} - b_{a,i} \end{bmatrix} \tag{4}$$

where $a^{-} = \frac{1}{2}(a_i + a_j)$. The first 6 dimensions are kinematic constraints, and the last 3 dimensions represent bias random walk. The information matrix Ω^{imu} of the motion constraint is jointly determined based on the time interval and sensor noise:

$$\Omega^{\text{imu}} = \text{diag}\left(\frac{1}{\sigma_p^2} I_3,\ \frac{1}{\sigma_v^2} I_3,\ \frac{1}{\sigma_{b_a}^2} I_3\right) \tag{5}$$

where $s = \frac{\Delta t}{dt_{ref}}$ $(dt_{ref} = 0.01\,s)$ is the time scaling factor. The position and velocity standard deviations take the larger of the time-scaled constraint and the acceleration noise constraint:

$$\sigma_p = max\left(10^{-3},\ max\left(\sigma_{\text{motion,pos}} \cdot s,\ \frac{1}{2}\sigma_a \Delta t^2\right)\right) \tag{6}$$

$$\sigma_v = max\left(10^{-3},\ max\left(\sigma_{\text{motion,vel}} \cdot s,\ \sigma_a \Delta t\right)\right) \tag{7}$$

The$\sigma_{b_a} = \max\left(10^{-6},\ \sigma_{acc_{bias_{rw}}} \sqrt{\Delta t}\right)$follows a random walk model. Specific values are provided in the Appendix.

When IMU world-frame acceleration is unavailable due to sensor frame dropout or abnormal jumps, the model automatically degrades to a constant-velocity model (motion_cv): $r_{i\to j}^{cv} = [p_j - p_i - v_i \Delta t;\ v_j - v_i;\ b_{a,j} - b_{a,i}]$

with $\sigma_p = \max(10^{-3},\ \sigma_{motion}, pos \cdot s)$、$\sigma_v = \max(10^{-3},\ \sigma_{motion}, vel \cdot s)$

The bias constraint uses a fixed standard deviation of 10^{-3} (since IMU acceleration is unavailable, it is not appropriate to impose time-increasing uncertainty on the bias). In granular flow scenarios, the motion constraints primarily maintain short-term continuity and reflect collision dynamic information.

For time step$k$ and base station A_a, the UWB ranging residual is defined as:

$$r_{k,a}^{\text{range}} = \| p_k - A_a \| - d_{k,a} \tag{8}$$

UWB in granular media faces occlusion, multipath, and NLOS propagation. Unlike preprocessing rejection or fixed weighting strategies, this paper computes residual statistics in real-time based on the current trajectory estimate during the optimization iteration and dynamically adjusts the information weight of each ranging

measurement. Specifically, for anchor a, the EWMA residual mean is defined with mean μ_a and variance ${s_a}^2$ with forgetting factor $\alpha = 0.05$:

$$\mu_a^{(t+1)} = (1-\alpha)\mu_a^{(t)} + \alpha \cdot r_{k,a}^{\text{range}} \tag{9}$$

$$s_a^{2(t+1)} = (1-\alpha)s_a^{2(t)} + \alpha \cdot (r_{k,a}^{\text{range}} - \mu_a^{(t)})^2 \tag{10}$$

For the centered residual $\bar{r}_{k,a} = r_{k,a}^{\text{range}} - \mu_a$ Cauchy-type adaptive weight is computed:

$$w_{k,a} = \frac{1}{1+\left(\frac{|\bar{r}_{k,a}|}{\sigma_a}\right)^2}, \quad \sigma_a = \max\left(0.15,\ 2.5\sqrt{s_a^2}\right) \tag{11}$$

The final information matrix of the ranging factor is jointly determined by the adaptive weight and the distance-dependent noise model:

$$w_{k,a} \leftarrow \begin{cases} 0.1 \cdot w_{k,a}, & |\bar{r}_{k,a}| > 1.0\text{m} \\ w_{k,a}, & \text{otherwise} \end{cases}, \quad w_{k,a} \leftarrow \text{clip}\left(w_{k,a},\ 0.05,\ 1.0\right) \tag{12}$$

This mechanism enables abnormal ranging measurements to be automatically and continuously down-weighted during optimization rather than being hard-rejected—the Cauchy weight function approaches 1 when the residual is small (normal observations fully participate in optimization), and smoothly decays to approximately 0.05 as the residual increases (abnormal observations are soft-suppressed). Meanwhile, EWMA adapts online to the dynamic changes of particle occlusion states, avoiding the adaptability issues of fixed-threshold methods in time-varying granular environments.

$$\Omega_{k,a}^{\text{range}} = \frac{w_{k,a}}{\sigma_{\text{range}}^2(d_{k,a})}, \quad \sigma_{\text{range}}(d) = \max(10^{-3},\ 0.12 + 0.01d) \tag{13}$$

High-damping motion in granular media should not exhibit high-frequency jitter; therefore, GP smoothing priors are introduced. For three consecutive frames $(k-1, k, k+1)$ and time intervals $(\Delta t_1, \Delta t_2)$, acceleration and jerk consistency constraints are imposed:

$$r_k^{\text{gp-pos}} = \frac{p_{k+1}-p_k}{\Delta t_2} - \frac{p_k - p_{k-1}}{\Delta t_1}, \quad \Omega = \frac{1}{0.9^2} I_3 \tag{14}$$

$$r_k^{\text{gp-vel}} = \frac{v_{k+1}-v_k}{\Delta t_2} - \frac{v_k - v_{k-1}}{\Delta t_1}, \quad \Omega = \frac{1}{3.0^2} I_3 \tag{15}$$

Three types of auxiliary constraints address the problems of weak observation, height drift, and endpoint divergence. Z-axis height anchoring: using the initial burial height $z_0 = 0.23\,m$, a strong constraint is applied at frame 0 $(\sigma = 0.001\,m)$, and a

soft constraint is applied to subsequent frames ($\sigma = 0.2\,m$). Zero-velocity constraint (ZUPT): for each frame j, if the frame acceleration magnitude $\| a_j^{world} \| < \tau_a$ and the angular velocity magnitude $\| \omega_j \| < \tau_{\omega\left(\tau_a = 0.20\frac{m}{s^2}, \tau_\omega = 0.20\frac{rad}{s}\right)}$, the frame is judged to be stationary, and $v_j = 0\left(\sigma_{zupt} = 0.08\frac{m}{s}\right)$, eliminating residual velocity during the stopping phase:

$$r_k^{\text{zupt}} = v_k, \quad \Omega_{\text{zupt}} = \frac{1}{0.08^2} I_3, \quad \forall k \in \{\, k \mid \text{ZUPT}_k = 1 \,\} \tag{16}$$

2.2.2 Initialization, Solving, and Evaluation Metrics

The initial position estimate is obtained by per-frame UWB inverse solution (requiring at least 4 valid anchors), velocity is obtained from adjacent differences, and the bias is initialized to zero. After constructing the factor graph, the TRF (Trust Region Reflective) algorithm is employed for global optimization ($Soft - L1$, f_{scale} = 1.0, convergence threshold 10^{-6}, maximum 200 iterations), utilizing analytical Jacobians for acceleration. Complete parameters are provided in the Appendix.

$$\text{RMSE} = \sqrt{\frac{1}{N}\sum_{k=1}^{N} \| p_k - p_k^{\text{ref}} \|^2} \tag{17}$$

The three-dimensional root mean square error (RMSE) for a single experiment is defined as the root mean square of the Euclidean distances between the estimated position and the reference position at each frame. The P95 error is the 95th percentile of all frame-wise three-dimensional position errors sorted in ascending order, used to characterize the high-error tail. The IMU dynamic response is characterized by the maximum magnitude of the world-frame acceleration (acceleration peak) and the maximum magnitude of the angular velocity (angular velocity peak) within a single experiment. The mean trajectory smoothness is defined as follows: the velocity sequence output by the factor graph optimization is differentiated once to obtain acceleration ($a = \frac{\Delta v}{\Delta t}$), and differentiated again to obtain jerk ($jerk = \frac{\Delta a}{\Delta t}$); the Euclidean norm of the three-dimensional jerk vector at each frame is computed and then averaged over all frames, with units of m/s³. This metric reflects the temporal continuity of the trajectory—a smaller value indicates smoother motion with fewer non-physical high-frequency jitter components. Error statistics across multiple experiments are reported

as mean ± standard deviation (mean ± SD). The per-axis RMSE is defined as $RMSE_d = \sqrt{\frac{1}{N}\Sigma_{\{k=1\}}^{N}\left(p_{\{k,d\}} - p_{\{k,d\}}^{ref}\right)^2}$, where $d \in \{x, y, z\}, p_{\{k,d\}}$ is the d-axis component of the estimated position at frame k, and $p_{\{k,d\}}^{ref}$ is the corresponding reference position component. From the relationship between the three-dimensional RMSE and the per-axis component RMSEs, it follows that $RMSE^2 = RMSE_x^2 + RMSE_y^2 + RMSE_z^2$. The directional dispersion contribution ratio is defined as $c_d = \frac{RMSE_d^2}{RMSE^2}(d \in \{x, y, z\})$, satisfying $\Sigma_d c_d = 1$, which quantifies the relative proportion of each coordinate axis direction in the total dispersion.

2.2.3 Constraint Mechanism Analysis

The design of the above constraint modules is based on the following mechanistic considerations. Fig. 4 illustrates the operating principles of the ranging noise model and motion prior. Fig. 4(a) shows the distance-dependent ranging noise model: UWB ranging error typically increases with propagation distance. In this paper, the ranging standard deviation is set as a linear function of distance, so that proximal base stations receive higher information weights, while distal base stations receive correspondingly lower weights due to longer paths and higher occlusion risk. This model provides the baseline scale for the subsequent NLOS adaptive weights. Fig. 4(b) compares the residual probability density before and after adding the acceleration prior: the original residual distribution is relatively wide, and after adding the prior, the residuals concentrate near zero, indicating that the motion prior can constrain the motion continuity between adjacent frames and suppress non-physical high-frequency jitter caused by abnormal ranging or weak observations.

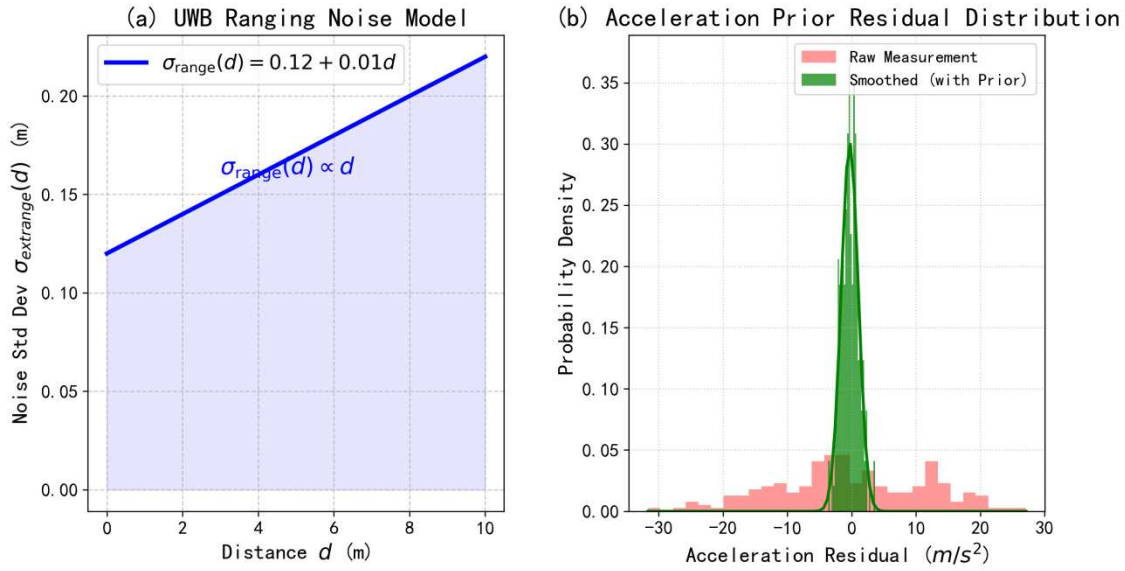


Fig. 4. Ranging noise model and motion prior residual distribution. (a) Model of ranging standard deviation as a function of distance; (b) Probability density distribution of acceleration residuals before and after adding the acceleration prior.

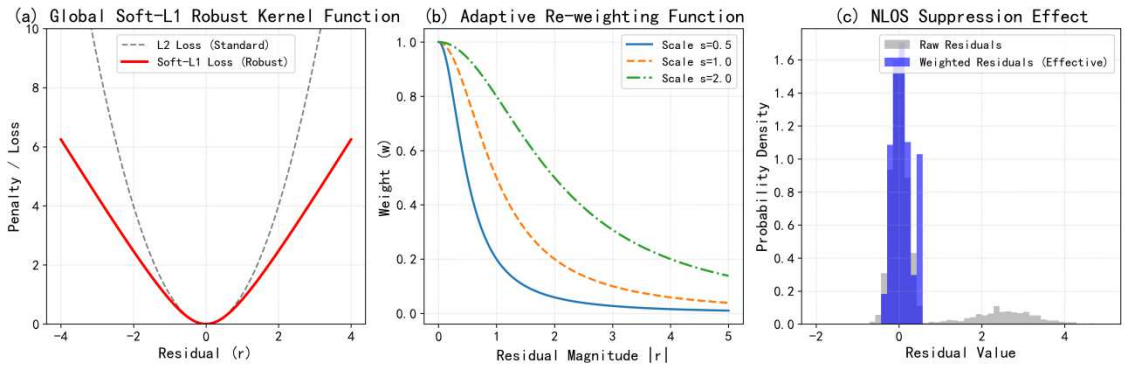


Fig. 5. Robust kernel function and NLOS adaptive down-weighting mechanism. (a) Comparison of Soft-L1 robust kernel and standard L2 loss; (b) Adaptive re-weighting function under different scale parameters; (c) Comparison of effective residual distributions before and after NLOS suppression.

Fig. 5 illustrates the robust kernel function and NLOS adaptive down-weighting mechanism. Fig. 5(a) compares the standard L2 loss with the Soft-L1 robust kernel: under L2 loss, the residual penalty grows rapidly with the square, and a small number of NLOS outliers can occupy excessive weight in the objective function; Soft-L1 approximates quadratic loss in the small-residual region and exhibits significantly slower penalty growth in the large-residual region, thereby weakening the dominance

of abnormal ranging measurements on the optimization. Fig. 5(b) shows the adaptive re-weighting function, where the weight decreases continuously as the residual increases, and the scale parameter controls the down-weighting intensity—UWB ranging degradation in granular media is typically continuous rather than binary, making continuous weighting more suitable than hard-threshold rejection. Fig. 5(c) compares the effective residual distributions before and after NLOS suppression: after weighting, the residuals converge toward zero and the long tail is compressed, indicating that the robust weights cause the optimization to rely more on observations with higher consistency.

2.3 Algorithm Validation

Before the motion experiments, static calibration was performed to confirm and correct the systematic positioning deviation of the stationary segment (Fig. 6). The three-axis positioning remained stable, with a systematic bias of approximately 0.037 m in the Z direction that did not diverge over time, indicating that the UWB ranging factors and initial position constraints in the factor graph optimization can effectively maintain positioning stability under stationary conditions.As shown in Fig. 6(a).

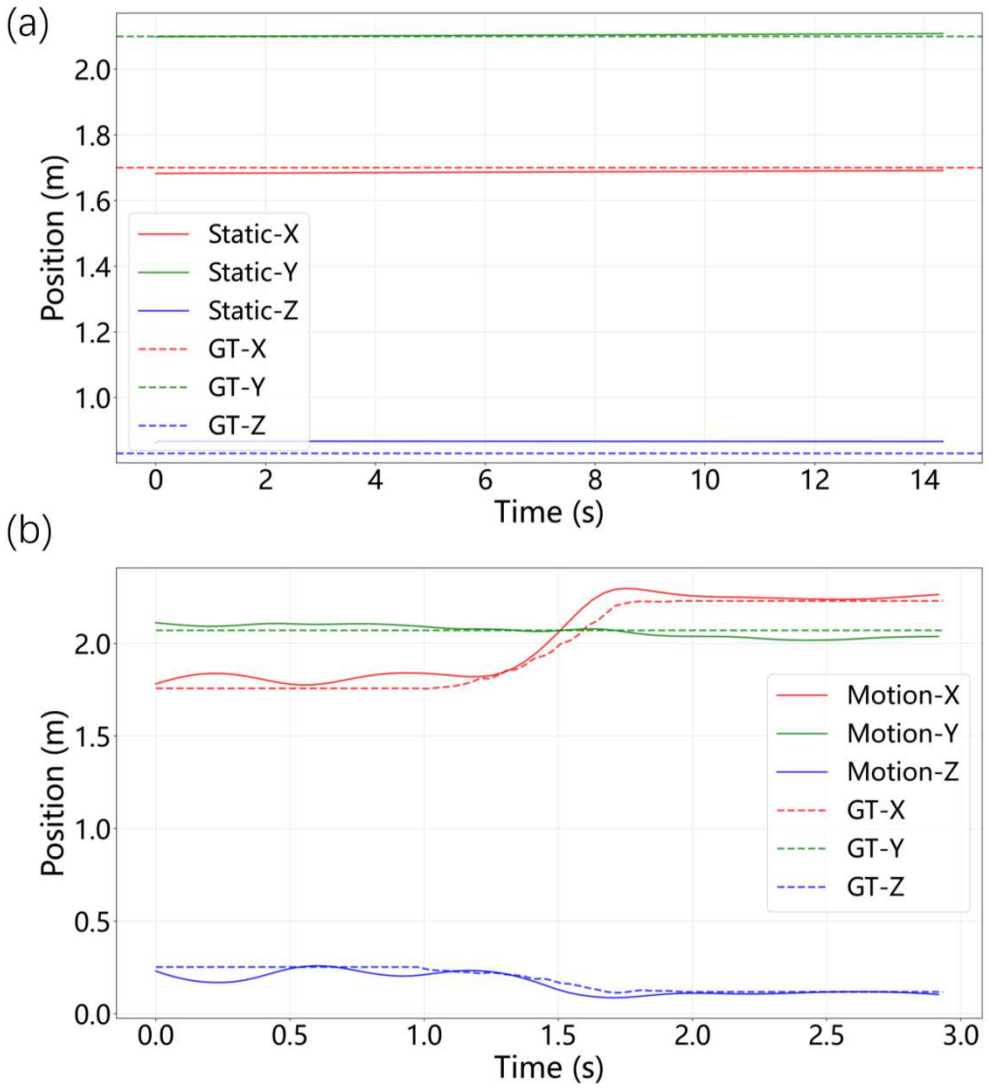


Fig. 6. Algorithm validation experimental results. (a) Position estimation results under static calibration conditions compared with reference positions; (b) Position estimation results under empty-chute motion conditions compared with video reference trajectory.

Fig. 6(b) shows the trajectory reconstruction results under empty-chute motion conditions. The X-direction reference trajectory begins to increase rapidly after approximately 1.2 s, and the algorithm-estimated curve accurately captures the startup and rapid migration processes, consistent with the reference trend. The Y-direction reference trajectory remains relatively stable, and the estimated results do not exhibit significant deviations. The Z-direction reference trajectory gradually decreases, and the estimated curve follows the overall trend, with some overshoot during the rapid motion

phase. Across all three directions, the algorithm achieves a trajectory reconstruction accuracy of 3D RMSE = 0.047 m under non-occluded conditions, indicating that the factor graph framework possesses the basic capability to continuously recover the bulk migration process of the measurement sphere under line-of-sight conditions.

The above empty-chute experiments validate the basic performance of the algorithm under ideal line-of-sight conditions. However, the core challenge of the granular flow internal measurement scenario lies in the degradation of UWB constraint quality under occluded conditions and the increase in motion path uncertainty. To establish the performance baseline of the algorithm under occluded conditions and quantify the improvement of the factor graph framework relative to traditional methods, a multi-method head-to-head comparison is conducted below under half-buried conditions.

Half-buried conditions provide moderate occlusion complexity and dynamic response intensity, making them suitable as a baseline condition for method comparison. This comparison uses the video tracking trajectory as the reference benchmark to compare the performance of four positioning methods on the same half-buried data: (1) Pure UWB—per-frame independent solution using only UWB ranging, representing the raw positioning performance without fusion; (2) EKF Fusion—the UWB/IMU extended Kalman filter tightly coupled method implemented according to [11], representing the recursive filtering route; (3) Basic Factor Graph—a basic factor graph using only UWB ranging factors and motion constraints, representing the baseline capability of the batch optimization framework; (4) Proposed—the complete factor graph method proposed in this paper, including adaptive NLOS weights, GP smoothing priors, and Z-direction auxiliary constraints. The comparison results are analyzed from two complementary perspectives: the cumulative distribution function (CDF) and the frame-by-frame error sequence.

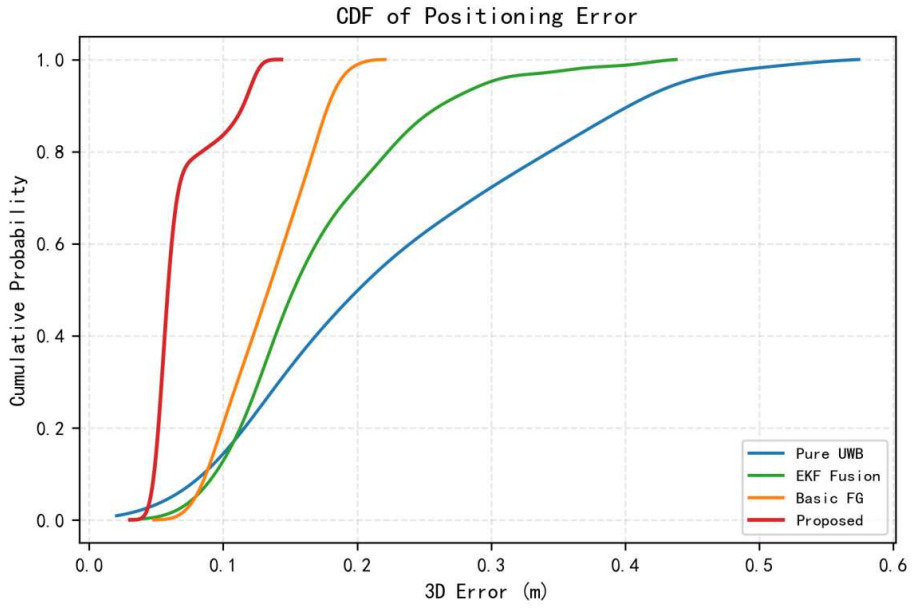


Fig. 7. Comparison of positioning error cumulative distribution functions (CDF) of the four positioning methods under half-buried conditions.

Fig. 7 presents the CDF of positioning errors for the four methods under half-buried conditions, where a curve closer to the upper-left corner indicates higher cumulative probability in the low-error region. The Pure UWB curve is most significantly shifted to the right (90% confidence corresponding to an error of approximately 0.45 m), reflecting the limitations of pure ranging positioning under particle occlusion. EKF Fusion reduces the 90% confidence error to approximately 0.30 m through IMU-assisted prediction. Basic Factor Graph slightly outperforms EKF in the low-error region by leveraging the global consistency of batch optimization. The Proposed method achieves a cumulative probability close to 1.0 in the low-error region (not exceeding 0.1 m) and essentially eliminates the high-error tail, demonstrating the synergistic enhancement of adaptive NLOS weights, GP smoothing priors, and Z-direction auxiliary constraints under half-buried occluded conditions.

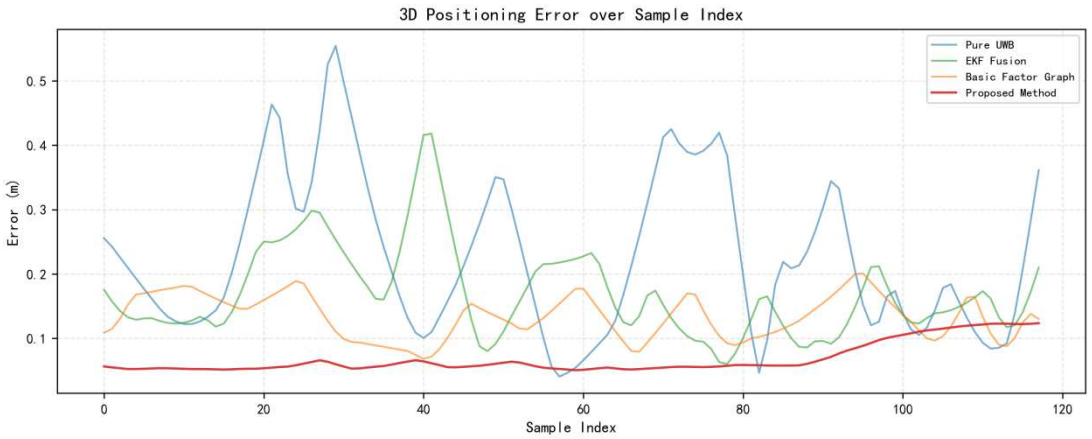


Fig. 8. Frame-by-frame 3D positioning error sequences of the four positioning methods under half-buried conditions.

Fig. 8 shows the temporal stability of the four methods from the perspective of frame-by-frame error sequences. Pure UWB exhibits severe error fluctuations, with frequent sudden spikes of 0.4–0.5 m, corresponding to moments when the measurement sphere is instantaneously occluded and the ranging link degrades to NLOS. EKF Fusion mitigates the extreme fluctuations, but still shows spikes of 0.2–0.3 m at NLOS transition moments, indicating that the recursive filter requires some time to recover convergence. The Basic Factor Graph error fluctuation amplitude and frequency are both significantly reduced, reflecting the inherent fault tolerance of batch optimization to individual abnormal observations. The Proposed method maintains errors within the range of 0.02–0.12 m throughout the entire process, with no large jumps, and achieves the best standard deviation among the four methods. Combining Fig. 7 and Fig. 8, the proposed complete factor graph method significantly outperforms the competing methods in both statistical distribution and temporal stability dimensions.

From the above empty-chute validation and half-buried method comparison, two interim conclusions can be drawn. First, the factor graph framework in this paper already possesses basic trajectory reconstruction capability under non-occluded conditions (empty-chute motion 3D RMSE = 0.047 m), and all constraint modules are designed based on physical mechanisms, ensuring the transferability of the method across different scenarios. Second, under the half-buried condition with partial occlusion, the proposed complete factor graph method (Proposed) significantly

outperforms Pure UWB, EKF Fusion, and Basic Factor Graph in both CDF and temporal dimensions. In particular, the cumulative probability in the low-error region (≤0.1 m) approaches 1.0, and there is no instantaneous divergence throughout the entire process—this advantage stems from the synergistic effect of the three improvements: adaptive NLOS weights, Z-direction auxiliary constraints, and GP smoothing priors. The above results constitute the methodological foundation and performance reference for the systematic ablation and self-consistency evaluation under more complex fully buried, mixed gradation, and wet conditions in Chapter 3.

3. Results and Discussion

3.1 Algorithm Ablation Experiment

To further verify the independent contributions and synergistic effects of each constraint module in the proposed trajectory reconstruction method in granular environments, ablation experiments are conducted under the 10 mm fully buried condition. This section uses the trajectory reconstructed by the complete model (Full, which simultaneously includes Z-direction auxiliary constraints, NLOS robust weights, and GP smoothing priors) as the comparison benchmark. The selection of this benchmark is based on the following considerations: the Full model has been proven to possess basic trajectory reconstruction capability in the algorithm validation of Section 2.3; all constraint modules are designed based on physical mechanisms rather than data-driven fitting; and the Full model exhibits optimal internal residuals and temporal continuity under comprehensive challenging conditions. Three algorithm configurations are set (Table 3): Baseline is the basic optimization model, without Z-direction auxiliary constraints, NLOS robust weights, or GP smoothing priors; B1 adds Z-direction auxiliary constraints (height anchoring and ZUPT zero-velocity constraint) on top of Baseline; B2 further adds NLOS robust weights on top of B1. The ablation experiment evaluates the independent contribution and cumulative effect of each module on trajectory reconstruction stability by comparing the trajectory deviation of each configuration relative to the Full model.

Table 3. Ablation Experiment Algorithm Configurations and Positioning Errors

Config.	Z-Constr.	NLOS Wt.	GP Smooth.	RMSE-3D (m)	RMSE-Z (m)	Smoothness	Primary Role
Baseline	No	No	No	0.122	0.113	21.625	Basic model
B1	Yes	No	No	0.032	0.015	21.596	Z-drift suppression
B2	Yes	Yes	No	0.016	0.010	21.528	Outlier ranging suppression
Full	Yes	Yes	Yes	0.0	0.0	0.405	Overall stability improvement

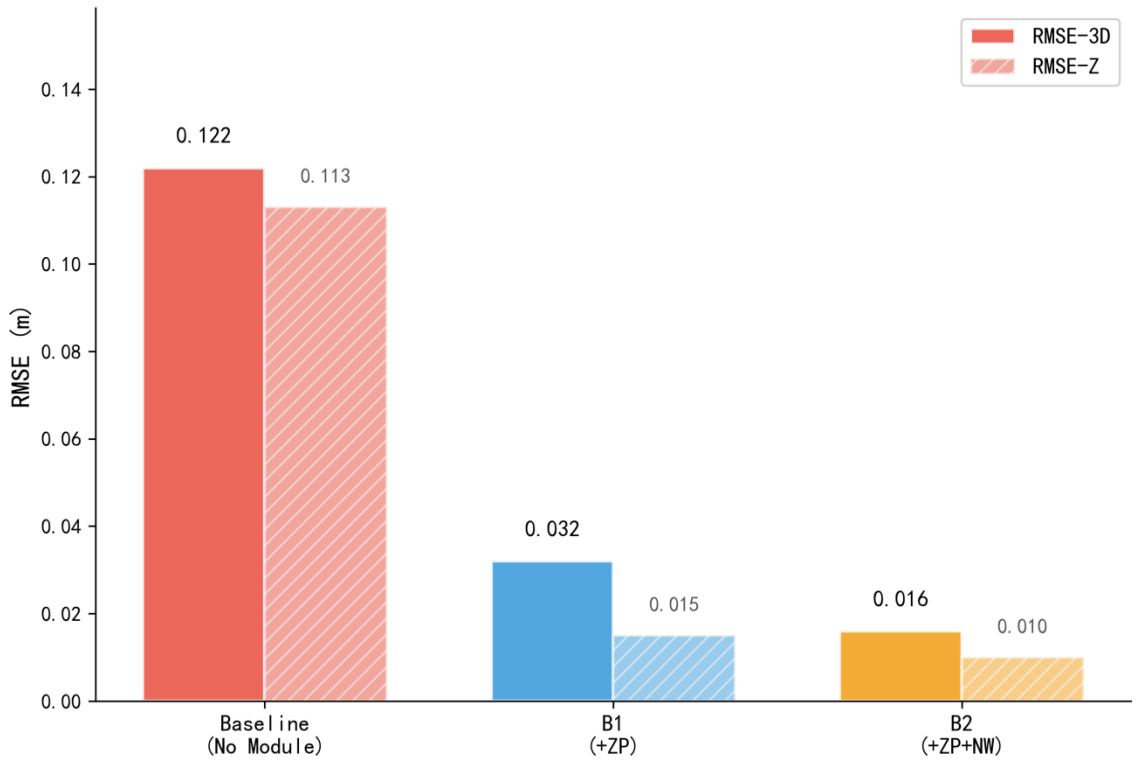


Fig. 9. Positioning error comparison of different algorithm configurations in the ablation experiment (relative to the Full model).

Fig. 9 presents the positioning error comparison of the three algorithm configurations relative to the Full model. The Baseline 3D RMSE is 0.122 m (with the largest contribution from the Z-direction, reaching 0.113 m), indicating that relying solely on basic UWB/IMU optimization without auxiliary constraints leads to

significant deviation from the Full model. After adding Z-direction auxiliary constraints, the B1 3D RMSE decreases to 0.032 m (approximately 74% reduction relative to Baseline), with the Z-direction decreasing to 0.015 m (approximately 87% reduction), validating the key role of height anchoring and ZUPT zero-velocity constraint in suppressing vertical drift. After further adding NLOS robust weights, the B2 3D RMSE further converges to 0.016 m, with balanced improvement across all directions. Overall, the Z-direction auxiliary constraint module alone contributes the major error reduction, and NLOS robust weights further tighten the trajectory deviation from the Full model on this basis.

From the perspective of trajectory smoothness, the three configurations without GP smoothing priors (Baseline, B1, and B2) all have smoothness means of 21.5–21.6, while the Full model smoothness mean decreases to 0.405, indicating that GP smoothing priors play a decisive role in enhancing trajectory temporal continuity and suppressing non-physical high-frequency jitter in particle-damped environments. The synergy of the three modules enables the complete model to simultaneously achieve the lowest deviation and optimal temporal smoothness under comprehensive challenging conditions.

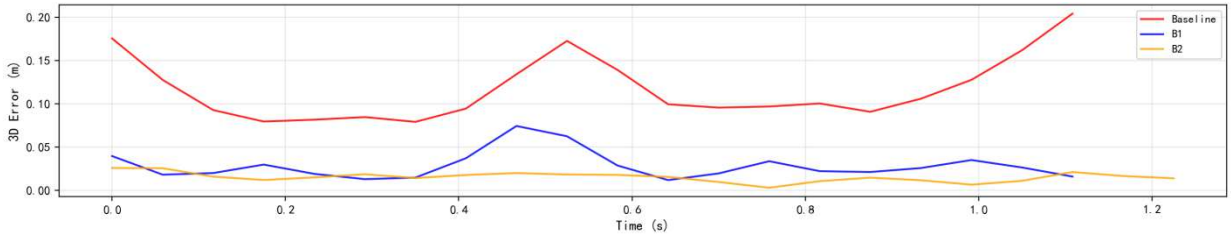


Fig. 10. Error temporal sequences of different algorithm configurations in the ablation experiment.

Fig. 10 further presents the local error temporal variation of the three algorithm configurations during the first 1.2 s. The Baseline has an initial error of approximately 0.175 m at t = 0 s, followed by large fluctuations in the range of 0.08–0.17 m, with slow convergence and poor stability. After adding Z-direction auxiliary constraints, B1 shows a significant reduction in initial error to approximately 0.04 m, remaining mostly within the range of 0.02–0.07 m, with significantly narrowed fluctuation amplitude.

After further adding NLOS robust weights on top of the Z-direction constraints, B2 performs best: the initial error is approximately 0.03 m, rapidly converging to approximately 0.015 m at t ≈ 0.1 s, and then stabilizing mostly within the range of 0.005–0.025 m. The three curves shift progressively downward and their fluctuation amplitudes narrow progressively, intuitively demonstrating the independent improvements of Z-direction auxiliary constraints and NLOS robust weights on optimization convergence speed and stability.

The above error temporal variation reveals the functional characteristics of each module: Z-direction auxiliary constraints primarily address the initial large deviation and slow convergence problems during the startup phase, reducing the error baseline from the 0.1 m level to below 0.05 m; NLOS robust weights further eliminate local fluctuations and spikes on this basis, maintaining the error within 0.025 m after approaching steady state. The combined effect of the two exceeds the linear superposition of single modules, reflecting complementary action.

The ablation results of Figs. 9 and 10 and Table 3 comprehensively demonstrate that, for the main trajectory degradation factors in granular media internal measurement (vertical weak observation, occlusion/NLOS abnormal ranging, and non-physical high-frequency jitter), the three types of constraint modules each have specialized functions: Z-direction auxiliary constraints mitigate vertical drift through height anchoring and ZUPT, reducing the 3D RMSE by approximately 74% with a single module; NLOS robust weights suppress abnormal ranging disturbances through adaptive down-weighting, further reducing the error by 50% on top of the Z-direction constraints; GP smoothing priors, through cross-frame acceleration and jerk consistency constraints, reduce the smoothness mean from approximately 21.5 to 0.405. The synergy of the three modules enables the Full model to simultaneously possess three major characteristics under comprehensive challenging conditions: low deviation, stable error temporal sequence, and high trajectory smoothness.

3.2 Influence of Granular Environment on Trajectory Self-Consistency

This paper uses the ensemble-mean trajectory of 30 repeated experiments under each condition as the statistical reference baseline. RMSE reflects the self-consistency

and repeatability of the trajectory---a smaller RMSE indicates a more convergent trajectory and more stable output. The definition of P95 is adjusted accordingly to the 95th percentile of the frame-wise deviations from the ensemble-mean trajectory within a single experiment. The calculation method for the IMU dynamic response metric remains unchanged. As shown in Fig. 11.

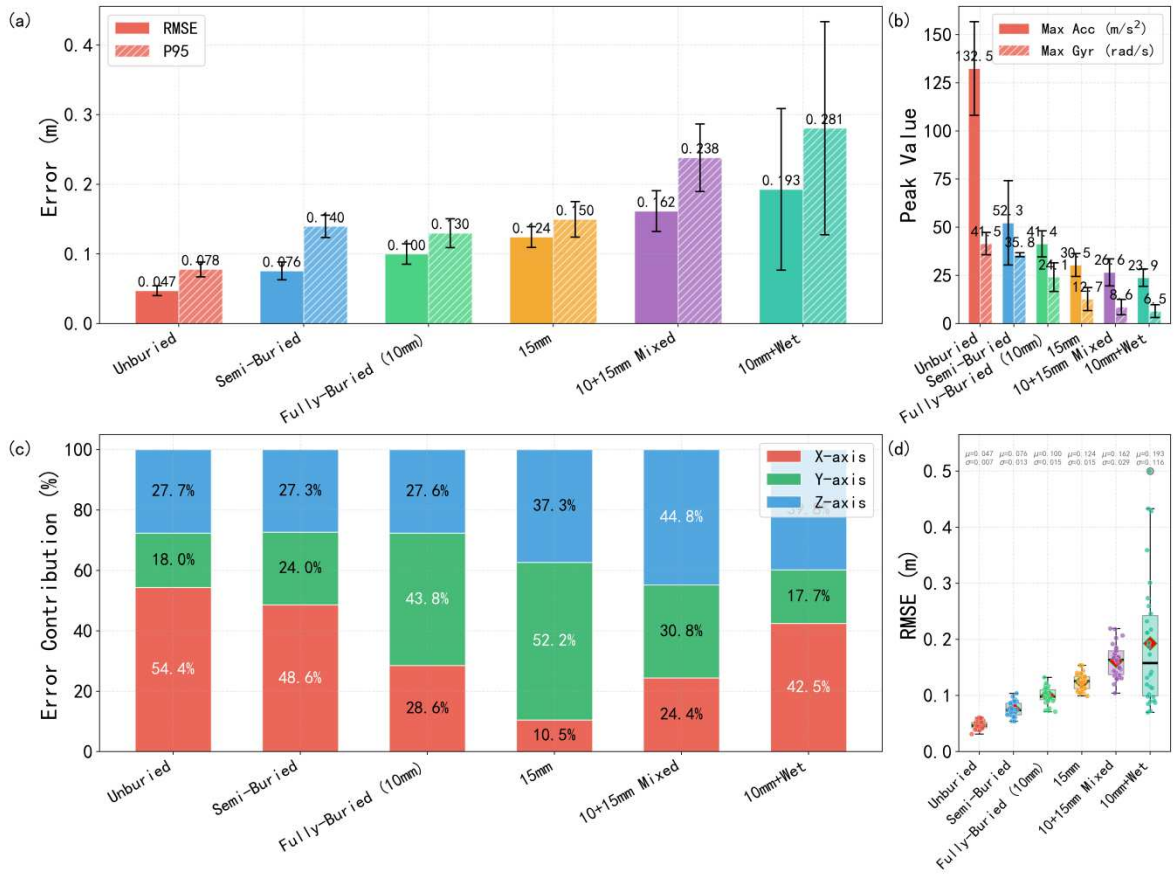


Fig. 11. Overview of self-consistency and dynamic response statistics for six conditions. (a) Comparison of 3D RMSE and P95 under six conditions (RMSE relative to ensemble-mean trajectory); (b) Comparison of IMU peak acceleration and peak angular velocity under six conditions; (c) Dispersion contribution ratios in X, Y, and Z directions; (d) 3D RMSE box plots and scatter distribution under six conditions.

Overall, as the granular environment becomes more complex, the IMU peak acceleration and peak angular velocity both decrease, while the 3D RMSE under the ensemble-mean reference increases synchronously, and P95 also rises from 0.078 m to

0.281 m, exhibiting a clear inverse trend. This indicates that granular motion impulses are not the main source of trajectory reconstruction error.

3.2.1 Influence of Burial State on Trajectory Self-Consistency

As shown in Figs. 11(a)(b), in the three groups of unburied, half-buried, and fully buried conditions, the IMU peak response drops sharply while trajectory dispersion increases, exhibiting a clear synchronous reversal. As the burial degree increases from unburied to full, the peak acceleration drops sharply from 132.5 m/s² to 41.4 m/s², and the peak angular velocity falls from 47.5 rad/s to 24.1 rad/s. Meanwhile, the RMSE increases from 0.047 m to 0.100 m, with the half-buried condition falling between the two (RMSE = 0.076 m). This inverse trend indicates that granular coverage does not reduce trajectory reconstruction quality by enhancing inertial impacts, but rather degrades the method's output consistency by weakening UWB absolute distance constraints and altering the contact boundary conditions.

From Fig. 11(c), it can be observed that under unburied and half-buried conditions, the X-direction dispersion contribution is relatively large (54.4% and 48.6%, respectively), indicating that trajectory dispersion under weak occlusion conditions mainly originates from the bulk migration process along the chute direction. Under the fully buried condition, the Y-direction dispersion contribution rises to 43.8%, indicating that lateral contact constraints and local particle rearrangement have an enhanced influence on trajectory stability after complete burial.

The typical trajectory comparison for the three conditions is shown in Fig. 12.

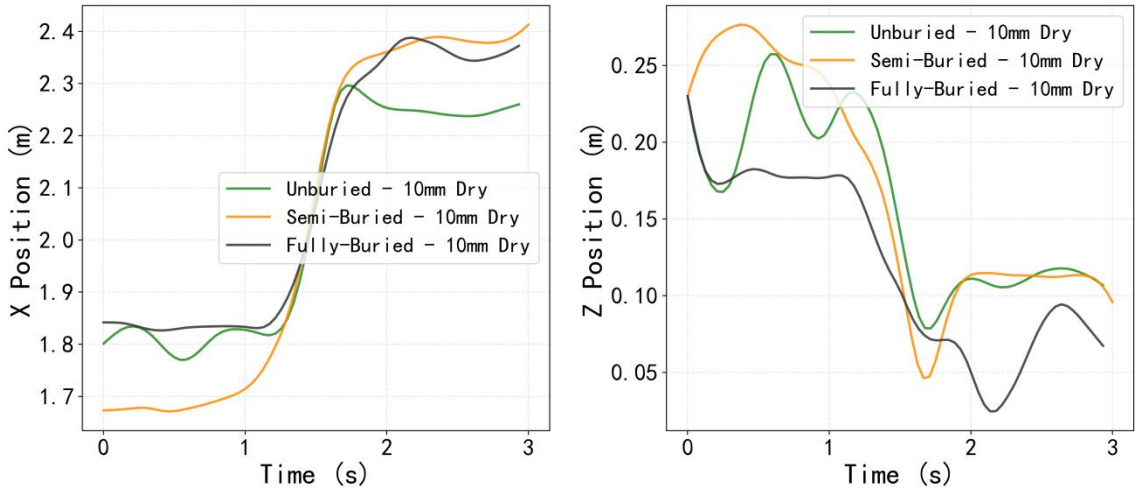


Fig. 12. Typical trajectory comparison under different burial states. (a) X-direction position-time curves; (b) Z-direction position-time curves.

The X-direction curves in Fig. 12(a) show that the reconstructed trajectories of the three conditions all exhibit the main process of startup–accelerated migration–stop, but the trajectory smoothness decreases with increasing burial degree. Deviations in the initial X coordinates of each condition due to differences in initial positioning conditions do not affect the comparison of the motion processes. In the Z-direction curves of Fig. 12(b), the vertical trajectories of the unburied and half-buried conditions are relatively flat in the later stages, while the fully buried condition exhibits a continuous downward drift, consistent with weakened UWB vertical constraints and increased uncertainty in Z-direction estimation.

In summary, the effect of burial state on trajectory reconstruction quality can be summarized as two parallel degradation pathways: first, deeper occlusion leads to degradation of UWB absolute ranging constraint quality; second, granular contact network constraints reduce IMU motion degrees of freedom, with high-frequency response being significantly suppressed.

3.2.2 Influence of Particle Size Gradation on Trajectory Self-Consistency

As shown in Fig. 11(a), under fully buried conditions, the RMSE increases from 0.100 m for 10 mm to 0.124 m for 15 mm and 0.162 m for mixed gradation (P95 reaches 0.238 m). Changes in particle size and gradation amplify trajectory dispersion, and a counterintuitive phenomenon is observed: the trajectory self-consistency of the large-

particle condition is actually worse. The IMU peak response also decreases correspondingly (Fig. 11(b)). From the perspective of directional contributions (Fig. 11(c)), the Y-direction contribution of the 15 mm condition reaches 52.2%, indicating prominent non-uniformity of lateral support from large particles. The mixed gradation condition has a combined X and Z direction contribution of approximately 88%, with the Z-direction exceeding 50%, reflecting the severe weakening of vertical stability by the non-uniform contact network. The above trends indicate that trajectory dispersion should be understood from the perspective of contact mechanics rather than the electromagnetic influence of the medium. In descending order of mixed particles, small particles, and large particles, the force chain stability of the environmental particles gradually decreases. The support structure formed by large particles is more sparse and the contact points are more discrete. The measurement sphere encounters more local voids and instantaneous contact instability events during migration, leading to reduced certainty of its motion path and increased trajectory differences between experiments, thereby reducing trajectory self-consistency.

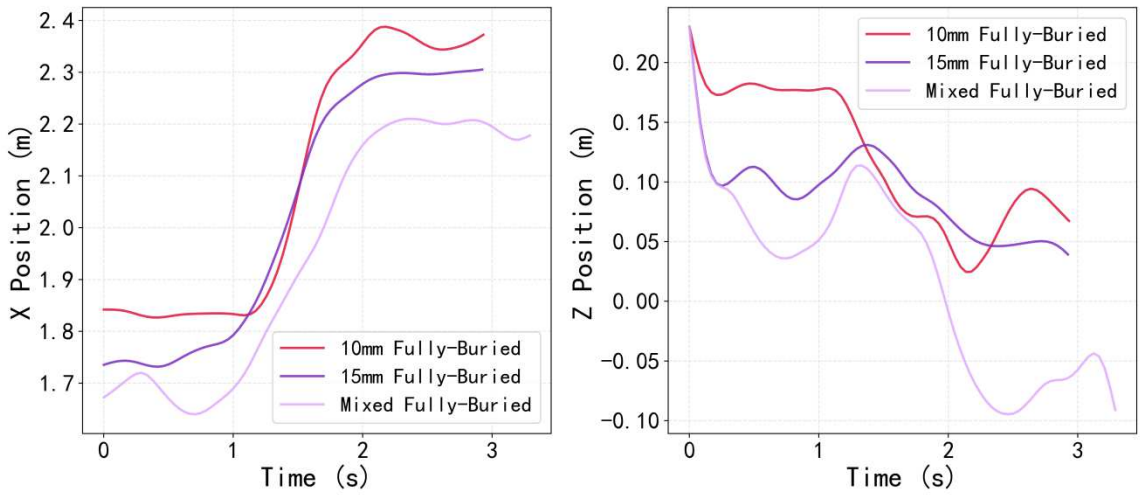


Fig. 13. Typical trajectory comparison under different particle size conditions. (a) X-direction position-time curves; (b) Z-direction position-time curves.

The typical trajectory comparison for the three particle size conditions is shown in Fig. 13. The X-direction curves in Fig. 13(a) show that the trajectory of the 10 mm condition is the smoothest, with clear migration characteristics. The overall migration amplitude of the 15 mm condition is slightly smaller. The mixed gradation condition

exhibits obvious fluctuations in the startup phase, with relatively delayed rapid migration. Deviations in the initial X coordinates of each condition due to differences in initial positioning conditions do not affect the comparison of the motion processes. In the Z-direction curves of Fig. 13(b), the Z-direction trajectory of the mixed gradation condition nearly crosses the physical boundary Z = 0 plane in the later stages, making it the only case of physically infeasible vertical trajectory. This phenomenon can be explained by the contact mechanics mechanism unique to mixed gradation: under the mixed condition of large and small particles, a continuous segregation process occurs within the particles—fine particles deposit toward the bottom under vibration and shear, while coarse particles rise toward the surface, causing the local vertical mass exchange and contact support structure of the measurement sphere's region to continuously reorganize. The IMU dynamic response data in Fig. 11(b) also corroborate this: the peak acceleration and peak angular velocity of the mixed gradation condition are the lowest among the three conditions, indicating that the measurement sphere experiences stronger contact constraints and motion freedom limitations in the gaps between large particles, rather than a free-flowing state. This discrete contact support causes physically infeasible offsets in the vertical estimation at individual frames.

The above mechanism analysis indicates that the influence of particle size gradation on trajectory self-consistency differs from that of burial state. Burial state mainly affects positioning quality by changing the UWB line-of-sight ratio, while particle size gradation mainly affects the dispersion between experiments by changing the certainty of the motion path. Although large particles weaken the electromagnetic absorption of the medium, they increase path randomness due to sparse support. This seemingly contradictory phenomenon is precisely the distinctive feature of internal measurement in granular flows.

3.2.3 Influence of Moisture Condition on Trajectory Self-Consistency

The physical motion mechanisms of dry and wet particles are fundamentally different, and it is theoretically impossible to directly compare their trajectories. We first evaluate the trajectory self-consistency of the condition itself, and then compare the trajectory dispersion and degradation mechanisms across conditions.

Taking the 10 mm fully buried condition as an example, the trajectory self-consistency of the wet condition is the poorest among all conditions. Under the ensemble-mean reference, the 3D RMSE reaches 0.193 m (P95 reaches 0.281 m), and the standard deviation of RMSE is the largest among all conditions (Fig. 11(d)), indicating higher and more divergent trajectory deviation. From the perspective of the dispersion contribution of each axis component (Fig. 11(c)), the combined X and Z direction contribution exceeds 85%, with significant dispersion in both the chute direction and the vertical direction. The IMU peak acceleration of the wet condition is 22.9 m/s² and the peak angular velocity is 6.5 rad/s (Fig. 11(b)), both at the lowest levels among the six conditions, reflecting that liquid bridge forces significantly suppress the motion of the measurement sphere. The above self-consistency data form a stark contrast with the dry particle condition of the same particle size (RMSE 0.100 m, peak acceleration 41.4 m/s², peak angular velocity 24.1 rad/s), indicating that the liquid bridge constraints and electromagnetic attenuation introduced by the moisture condition significantly amplify trajectory dispersion and markedly weaken IMU dynamic response.

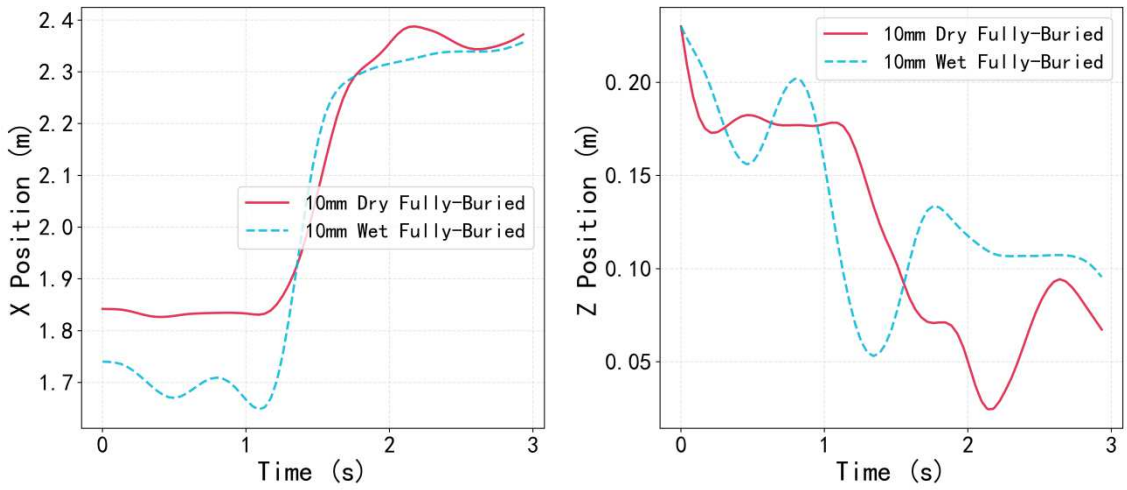


Fig. 14. Typical trajectory comparison under wet conditions. (a) X-direction position-time curves; (b) Z-direction position-time curves.

Fig. 14 shows the typical reconstructed trajectories under wet and dry particle conditions. The morphological differences between the two conditions' trajectories reflect the significant differences in the physical motion paths of the measurement

sphere under dry and wet conditions. The local fluctuation frequency of the wet condition trajectory is higher, and its trajectory smoothness is significantly lower than that of the dry particles, also reflecting the more complex mechanical mechanisms within the granular system under wet conditions.

From the analysis of measurement results, the degradation of trajectory self-consistency under wet conditions can be attributed to the coupled action of two pathways: contact mechanics and electromagnetic propagation. At the contact mechanics level, liquid bridge cohesive forces enhance normal adhesion between particles and introduce rotational constraints: the IMU peak angular velocity of the wet condition (6.5 rad/s) is less than one-third of that of the dry particle condition of the same particle size (24.1 rad/s), indicating that the degree of restriction of liquid bridge forces on the rotational freedom of the measurement sphere far exceeds the constraint capability of the collision-friction mechanism. The transient rupture and reformation of liquid bridges also cause stagnation and discontinuous migration of the measurement sphere motion, increasing path randomness, which is the contact mechanics root of the largest RMSE standard deviation of the wet condition among the six conditions. At the electromagnetic propagation level, the relative permittivity of water (approximately 80) is much higher than that of POM (approximately 3.7), significantly exacerbating UWB signal attenuation and complicating multipath propagation, further degrading the ranging constraint quality.

3.2.4 Trajectory Self-Consistency Degradation Mechanism

Synthesizing the above experimental results, the degradation mechanism of trajectory self-consistency for burial degree and particle size gradation depends on the granular contact network, while the addition of water not only strengthens the contact forces between particles (i.e., the effective viscosity) but also causes electromagnetic signal attenuation. The burial degree externally changes the UWB line-of-sight ratio and ranging constraint quality. Particle size gradation affects path repeatability through the spatial distribution characteristics of force chains. Under a single particle size, the flow regime of small particles tends to be more liquid-like, with trajectories exhibiting greater continuity and self-consistency; the internal support points of large particles are

more sparse; while mixed gradation involves mass exchange in the Z-direction within the particles, increasing path randomness. The moisture condition simultaneously acts on both contact mechanics and electromagnetic propagation pathways. The presence of liquid bridges makes the mechanical interaction structure between particles more complex, enhancing path uncertainty, while the dielectric properties of water exacerbate UWB signal attenuation. The coupled degradation makes the dispersion of the wet condition the highest among all conditions.

The data under three environmental variables collectively reveal one result: the reduction in IMU dynamic response is not the cause of increased trajectory dispersion, but rather a concomitant phenomenon of intensified granular environmental constraints. The true driving factor of internal measurement dispersion in granular flows is the weakening of spatial constraint quality and the decline in motion path certainty, rather than the inertial impact itself.

Viewed from the unified perspective of contact structure determining path certainty, the applicability of the method is constrained by the following conditions. (1) The burial state determines the basic properties of the UWB propagation path. The transition from unburied to fully buried significantly increases the NLOS ratio, which is the most direct factor affecting trajectory reconstruction accuracy. (2) Particle size and gradation change path certainty through the spatial distribution characteristics of force chains. Continuous support from small particles is conducive to trajectory stability, while sparse support from large particles and the discrete contact structure of mixed gradation increase path uncertainty. (3) The moisture condition simultaneously acts on contact mechanics and electromagnetic propagation. Liquid bridge constraints limit rotational freedom and alter force transmission paths, while the dielectric constant of water, much higher than that of the particle material, exacerbates UWB attenuation. The coupling of these two effects results in the highest trajectory dispersion.

The adaptive NLOS weights, GP smoothing priors, and Z-direction auxiliary constraints proposed in this paper can effectively mitigate ranging anomaly disturbances and vertical drift, but their ability to compensate for path uncertainty caused by contact network complexity is limited. Future research should enhance UWB

penetration and multipath resolution capability at the hardware level and introduce signal quality discrimination indicators such as Received Signal Strength Indicator (RSSI) and Channel Impulse Response (CIR) to distinguish the respective contributions of mechanical constraints and electromagnetic degradation.

4. Conclusion

This paper proposes a factor graph optimization algorithm integrating Z-direction auxiliary constraints, NLOS robust weights, and GP smoothing priors, achieving three-dimensional trajectory reconstruction and dispersion degradation law analysis of the intrusive measurement sphere in complex granular environments. Validated through 6 independent conditions and 180 repeated experiments, the ablation experiment shows that Z-direction auxiliary constraints reduce the trajectory deviation relative to the Full model by approximately 74%, NLOS robust weights reduce it by approximately 50%, and GP smoothing priors reduce the trajectory smoothness from 21.5 m/s^3 to 0.405 m/s^3. Under half-buried conditions, the RMSE of the Full algorithm is 0.076 m, and the 90% positioning error is reduced from 0.45 m (Pure UWB) to within 0.10 m. Multi-condition measurements reveal that trajectory self-consistency degradation follows the unified logic of "contact structure–path certainty–dispersion": burial degree increases RMSE by changing the UWB line-of-sight ratio; particle size gradation affects path certainty through force chain spatial distribution, with the mixed gradation fully buried condition reaching 0.162 m (P95 = 0.238 m); the moisture condition simultaneously causes degradation through both contact mechanics and electromagnetic propagation pathways, with RMSE rising to 0.193 m. The inverse evolution phenomenon in all six conditions—IMU dynamic response decreases while trajectory dispersion increases—indicates that the true driving factor of self-consistency degradation is path uncertainty caused by the contact network structure.

5. Statements and Declarations

5.1 Funding

This work was supported by the National Natural Science Foundation of China (Nos. 12372384 and 12072200) and the National Key Research and Development Program of China (No. 2022YFF0607701).

5.2 Competing Interests

The authors have no relevant financial or non-financial interests to disclose.

References

[1] Wang B D, Song J, Li R, et al. A novel particle tracking velocimetry method for complex granular flow field[J]. Chinese Physics B, 2020, 29(1):014207. https://doi.org/10.1088/1674-1056/ab5936

[2] Farmani Z, Wieringa J A, Dijksman J A. Integrating flow testing and particle imaging: Advances in characterising granular flows[J]. KONA Powder and Particle Journal, 2025, 42:57-78. https://doi.org/10.14356/kona.2025014

[3] Liang J, Cai S, Xu C, et al. DeepPTV: Particle tracking velocimetry for complex flow motion via deep neural networks[J]. IEEE Transactions on Instrumentation and Measurement, 2022, 71:1-13. https://doi.org/10.1109/tim.2021.3120127

[4] Guillard F, Marks B, Einav I. Dynamic x-ray radiography reveals particle size and shape orientation fields during granular flow[J]. Scientific Reports, 2017, 7:8155. https://doi.org/10.1038/s41598-017-08573-y

[5] Windows-Yule C R K, Seville J P K, Ingram A, et al. Positron emission particle tracking of granular flows[J]. Annual Review of Chemical and Biomolecular Engineering, 2020, 11:367-396. https://doi.org/10.1146/annurev-chembioeng-011620-120633

[6] Clarke D A, Hogendoorn W, Penn A, et al. Magnetic resonance imaging in granular flows: An overview of recent advances[J]. Particuology, 2025, 101:18-32. https://doi.org/10.1016/j.partic.2023.08.007

[7] Köstler S, Zhao J, Lyu C, et al. Embedded inertial sensor for tracking projectile impact on granular media[C]//EPJ Web of Conferences. 2021, 249:15007. https://doi.org/10.1051/epjconf/202124915007

[8] Jiao J J, Sun Y H, An Y, et al. Design and calibration of spherical particles with embedded inertial measurement unit: Preserving kinematic equivalence[J]. Acta Mechanica Sinica, 2026, 42:324749.
https://doi.org/10.1007/s10409-025-24749-x

[9] Xie Y, Melville B W, Shamseldin A Y, et al. Smart sediment particle: A novel approach to investigating fluvial bed entrainment using instrumented sensors[J]. International Journal of Sediment Research, 2023, 38(1):66-82.
https://doi.org/10.1016/j.ijsrc.2022.08.003

[10] Černilová B, Kuře J. The IMU sensor for in-situ 3D movement monitoring of particulate matter[C]//Engineering Proceedings. 2024, 82(1):57.
https://doi.org/10.3390/ecsa-11-20509

[11] Zou A R, Hu W W, Luo Y H, et al. An improved UWB/IMU tightly coupled positioning algorithm study[J]. Sensors, 2023, 23(13):5918.
https://doi.org/10.3390/s23135918

[12] Sui X, Song J, Wang C, et al. UWB/MEMS IMU integrated positioning method based on NLOS angle discrimination and MAP constraints[J]. Scientific Reports, 2024, 14:19879.
https://doi.org/10.1038/s41598-024-70802-y

[13] Leitch S G, Ahmed Q Z, Abbas W B, et al. On indoor localization using WiFi, BLE, UWB, and IMU technologies[J]. Sensors, 2023, 23(20):8598.
https://doi.org/10.3390/s23208598

[14] Ji P F, Duan Z X, Xu W S. A combined UWB/IMU localization method with improved CKF[J]. Sensors, 2024, 24(10):3165.
https://doi.org/10.3390/s24103165

[15] Cheng L, Liu K. INS/UWB fusion localization algorithm in indoor environment based on variational Bayesian and error compensation[J]. Journal of the Franklin Institute, 2024, 361(17):107204.
https://doi.org/10.1016/j.jfranklin.2024.107204

[16] Wang S, Ahmad N S. Improved UWB-based indoor positioning system via NLOS classification and error mitigation[J]. Engineering Science and Technology, an International Journal, 2025, 63:101979.
https://doi.org/10.1016/j.jestch.2025.101979

[17] Ren M, Wei J, Qin J, et al. Attention-based LSTM framework for robust UWB and INS integration in NLOS environments[J]. Scientific Reports, 2025, 15:21637.
https://doi.org/10.1038/s41598-025-05501-3

[18] Wang H Y, He J X, Cui L Z. An advanced indoor localization method based on xLSTM and residual multimodal fusion of UWB/IMU data[J]. Electronics, 2025, 14(13):2730.
https://doi.org/10.3390/electronics14132730

[19] Zhou Z, Xu Z, Xia J. Deep learning optimization positioning algorithm based on UWB/IMU fusion in complex indoor environments[J]. Physical Communication, 2025, 71:102702.
https://doi.org/10.1016/j.phycom.2025.102702

[20] Liu Y, Hu E, Chen Y, et al. Neurodynamic robust adaptive UWB localization algorithm with NLOS mitigation[J]. Scientific Reports, 2025, 15:16552.
https://doi.org/10.1038/s41598-025-99150-1

[21] Zhang F Y, Li J, Zhang X Q, et al. Indoor fusion positioning based on IMU-ultrasonic-UWB and factor graph optimization method[EB/OL]. arXiv, 2025.
https://doi.org/10.48550/arXiv.2503.12726

[22] Wang R, Xu C, Li R, et al. Cooperative localization and mapping based on UWB/IMU fusion using factor graphs[J]. IEEE Sensors Journal, 2024, 24(14):21931-21940.
https://doi.org/10.1109/jsen.2023.3316278

[23] Fan G, Wang Q, Yang G, et al. RFG-TVIU: Robust factor graph for tightly coupled vision/IMU/UWB multi-sensor fusion[J]. Frontiers in Neurorobotics, 2024, 18:1343644.
https://doi.org/10.3389/fnbot.2024.1343644

[24] Kuang Y, Hu T, Ouyang M, et al. Tightly coupled LiDAR/IMU/UWB fusion via resilient factor graph for quadruped robot positioning[J]. Remote Sensing, 2024, 16(22):4171.
https://doi.org/10.3390/rs16224171

[25] Mahony R, Hamel T, Pflimlin J M. Nonlinear complementary filters on the special orthogonal group[J]. IEEE Transactions on Automatic Control, 2008, 53(5):1203-1218.
https://doi.org/10.1109/tac.2008.923738

[26] Cheng K, Hou M, Li T, et al. Tracking the motion of an intruder particle in a three-dimensional granular bed on-board the Chinese space station[J]. Microgravity Science and Technology, 2024, 36:15.
https://doi.org/10.1007/s12217-024-10102-2

[27] Cheng K, Hou M, Sun W, et al. Trajectories of a magnetic sphere in a shaken three-dimensional granular bed under low gravity[J]. Scientific Data, 2025, 12:238.
https://doi.org/10.1038/s41597-025-04517-8

[28] Guo H, Song S, Yin H, et al. Optimization of UWB indoor positioning based on hardware accelerated Fuzzy ISODATA[J]. Scientific Reports, 2024, 14:17985.
https://doi.org/10.1038/s41598-024-68998-0

[29] Lee B, Choi J, Jeong S, et al. Comprehensive outdoor UWB dataset: Static and dynamic measurements in LOS/NLOS environments[J]. Scientific Data, 2025, 12:1532.
https://doi.org/10.1038/s41597-025-05887-9

[30] De Cock C, Tanghe E, Joseph W, et al. Robust IMU-based mitigation of human body shadowing in UWB indoor positioning[J]. Sensors, 2023, 23(19):8289.
https://doi.org/10.3390/s23198289

[31] Cheng L, Chen Y, Guan J. INS/UWB multi-sensor integrated localization scheme in indoor LOS/NLOS environments based on MEF-GPDAF[J]. Computers & Electrical Engineering, 2024, 116:109180.
https://doi.org/10.1016/j.compeleceng.2024.109693

[32] Tu C, Zhang J, Quan Z, Ding Y. UWB indoor localization method based on neural network multi-classification for NLOS distance correction[J]. Sensors and Actuators A: Physical, 2024, 379:115904. https://doi.org/10.1016/j.sna.2024.115904

Appendix: Core Algorithm Parameters

UWB ranging factor (Eq. 8) Jacobian with respect to positionp_k:

$$\frac{\partial r_{k,a}^{\text{range}}}{\partial p_k} = \frac{(p_k - A_a)^\top}{\|p_k - A_a\|} \in \mathbb{R}^{1\times 3} \tag{18}$$

IMU motion factor (Eq. 4) Jacobian with respect to adjacent states:(x_i, x_j)

$$\frac{\partial r_{i\to j}^{\text{imu}}}{\partial x_i} = \begin{bmatrix} -I_3 & -\Delta t \cdot I_3 & \frac{1}{2}\Delta t^2 \cdot I_3 \\ 0 & -I_3 & \Delta t \cdot I_3 \\ 0 & 0 & -I_3 \end{bmatrix}, \quad \frac{\partial r_{i\to j}^{\text{imu}}}{\partial x_j} = \begin{bmatrix} I_3 & 0 & 0 \\ 0 & I_3 & 0 \\ 0 & 0 & I_3 \end{bmatrix} \tag{19}$$

GP smoothing factor (Eq. 14) Jacobian with respect to three-frame positions (p_{k-1}, p_k, p_{k+1})

$$\frac{\partial r_k^{\text{gp-pos}}}{\partial [p_{k-1}, p_k, p_{k+1}]} = \left[\frac{1}{\Delta t_1} I_3, \quad -\left(\frac{1}{\Delta t_1} + \frac{1}{\Delta t_2}\right) I_3, \quad \frac{1}{\Delta t_2} I_3\right] \tag{20}$$

The complete parameter settings referenced in the above factor definitions are summarized in Table 4.

Table 4. Core Algorithm Parameter

Category	Parameter	Value	Category	Parameter	Value
UWB	sigma_uwb_range_base	0.12 m	Smoothing	sigma_gp_pos_acc	0.9 m/s²
UWB	sigma_uwb_range_k	0.01	Smoothing	sigma_gp_vel_jerk	3.0 m/s³
IMU	sigma_acc	1.2 m/s²	ZUPT	sigma_zupt_vel	0.08 m/s
Motion	sigma_motion_pos	0.05 m	Z-axis	sigma_init_z	0.001 m
Motion	sigma_moti	0.30 m/s	Z-axis	sigma_glob	0.2 m

Category	Parameter	Value	Category	Parameter	Value
	on_vel			al_z	
Motion	motion_dt_ref	0.01 s	Boundary	sigma_boundary_pos	0.20 m
Bias	sigma_acc_bias_rw	1×10^{-4}	Boundary	sigma_boundary_vel	1.0 m/s
NLOS	nlos_ewma_alpha	0.05	NLOS	nlos_residual_floor	0.15 m
NLOS	nlos_gate_hard	1.0 m	NLOS	nlos_min_weight	0.05
Solver	loss	soft_l1	Solver	f_scale	1.0
Solver	max_nfev	200/80	Solver	ftol/gtol/xtol	$10^{-6}/10^{-4}$